*Geophysical Research Letters*

Supporting Information for

# Continuum-scale Predictions of Solute Transport Derived from Pore-scale Velocity Distributions

by G.M. Porta[1], B. Bijeljic[2], M.J. Blunt[1,2] and A. Guadagnini[1,3]

[1]Dipartimento di Ingegneria Civile e Ambientale, Politecnico di Milano, Piazza L. Da Vinci 32, 20133 Milano, Italy

[2]Department of Earth Science and Engineering, Imperial College, London, SW7 2AZ, UK

[3]Department of Hydrology and Water Resources, University of Arizona, Tucson, AZ 85721,

## Contents of this file



Supplementary material S1 provides details on the characterization of the bead pack and the sandstone samples at the pore-scale and image segmentation.

Supplementary material S2 provides the details on fluid flow pore-scale numerical simulations. We detail the implemented equations, the meshing and convergence criteria. We also discuss the flow conditions characterizing the flow field used for pore-scale transport simulation and employed to characterize model 2.

Supplementary material S3 provides all details underlying the derivation of equations (9)-(11).

## Text S1. Characterization of the bead pack and the sandstone sample and image segmentation

The bead pack image is based on existing data for the coordinates of the centers of equally-sized spherical grains in a random close packing, as originally measured by *Finney* [1970]. The segmentation into the pore and solid voxels has been performed by *Prodanović and Bryant* [2006]. The dry-scan image of Bentheimer sandstone was acquired by an Xradia Versa micro-CT scanner (provided by iRock Technologies) on a cylindrical core of 5 mm diameter and 25 mm length. The image was segmented into pore and solid voxels using a seeded watershed algorithm based on the three-dimensional gradient magnitude and grey-scale value of each voxel. All image processing was performed using the Avizo Fire 7.0 program (VSG; www.vsg3d.com).

Characteristic attributes of the imaged geometry of the two samples are listed in Table S1. The bead pack image size is 300 × 300 × 300 voxels, voxel size $\hat{\Delta}$ being equal to 2 μm yielding a total size of 0.6 mm × 0.6 mm × 0.6 mm. The Bentheimer image size is 300 × 300 × 300 voxels; here, $\hat{\Delta} = 3\mu\text{m}$, resulting in a total size of 0.9 mm × 0.9 mm × 0.9 mm. Note that both images are characterized by a value of $\hat{L}_{im,i}$ which is constant along each direction $i = x$, $y$, and $z$. Porosity $\phi$ is equal to 35.9% and 21.5%, respectively for the bead pack and the Bentheimer sandstone image.

The quantity $\hat{\lambda}_G$ represents the range of the variogram of the indicator function $G(\mathbf{x})$ ( $G(\mathbf{x}) = 0$, 1 respectively for $\mathbf{x}$ belonging to the solid grains and fluid phase) estimated from pore-scale imaging. Values of $\hat{\lambda}_G$ listed in Table S1 are estimated by considering an exponential model to interpret the variogram of $G(\mathbf{x})$ reported by *Bijeljic et al.* [2013a]. We estimate $\hat{\lambda}_G$ = 48 μm for the bead pack sample. This value is close to the average pore size ( $\hat{L} = \hat{d}\phi/(1-\phi) = 56$ μm) which can be derived analytically and which we employ to characterize the length scale in the bead pack sample (see Section 2.2). We find $\hat{\lambda}_G$ = 121 μm for the sandstone sample. In the absence of analytical formulations of the kind associated with the bead pack to determine the characteristic pore size in a consolidated rock, we assume $\hat{L} = \hat{\lambda}_G$ for our analysis. Note that our estimates $\hat{\lambda}_G$ are significantly smaller than the total image size $\hat{L}_{im}$ for both considered porous media. This result suggests that the sample size is appropriate to represent geostatistically the geometrical attributes of the two media.

## Text S2. Pore-scale flow simulation

To compute flow field on the bead pack and sandstone image voxels we solve the mass conservation and Navier-Stokes equations for incompressible flow using a standard finite-volume method for discretization that is implemented in OpenFoam

$$\nabla \cdot \hat{\mathbf{u}}_{PS} = 0 \tag{S1}$$

$$\hat{\rho}\left(\frac{\partial \hat{\mathbf{u}}_{PS}}{\partial \hat{t}} + \hat{\mathbf{u}}_{PS} \cdot \hat{\nabla}\hat{\mathbf{u}}_{PS}\right) = -\hat{\nabla}\hat{p} + \hat{\mu}\hat{\nabla}\hat{\mathbf{u}}_{PS} \tag{S2}$$

where $\hat{\mathbf{u}}_{PS}$ is the velocity vector, $\hat{\mu}$ is the viscosity of water (0.001 Pa s), $\hat{\rho}$ is density of water (1000 kg/m$^3$) and $p$ is pressure. Pressure and velocity are solved iteratively based on the pressure implicit with splitting of operators (PISO) algorithm of *Issa* [1986]. No slip condition is imposed on solid boundaries. This method has been previously used in pore-scale simulation of flow, transport and reaction on voxelized images [*Raeini et al.*; 2012; *Bijeljic et al*., 2013a,b; *Siena et al.*, 2014; *Muljadi et al.*, 2015; *Pereira-Nunes et al.*, 2015; *Alhashmi et al.*, 2015].

Meshing is performed in Cartesian coordinates where each pore voxel represents a grid block. The mesh resolution coincides with the voxel size. The convergence criterion was defined to be fulfilled when the maximum change (per iteration) in velocities at the voxel centers was less than $10^{-6}$ of the average velocity of all image voxels [*Muljadi et al.*, 2015].

The code has been tested for grid convergence [*Muljadi et al.*, 2015] for a bead pack and a carbonate image (Estaillades limestone). For the bead pack image used in this work (300 × 300 × 300 image with 2μm voxel size) we checked grid independence of the results by subdividing each voxel into eight smaller voxels to obtain the new image consisting of 600 × 600 × 600 voxels, where new voxel size is 1μm. The Darcy permeabilities computed in the fine grids for both bead pack and limestone images compared well with those computed in the original coarser grids, with a difference of less than 5%.

In this work we solve equations (S1)-(S2) by imposing a pressure gradient along *x*. This boundary condition is imposed to set a fixed value of the average velocity $\hat{U}$ along the *x*-direction. Average pore velocities, $\hat{U}$ , in the pore-scale simulation are the same as in the experiment by *Scheven et al.* [2005], i.e., $\hat{U} = 0.91$ mm/s for bead pack and $\hat{U} = 1.03$ mm/s for Bentheimer sandstone (see also Section 2.2).

As described in *Bijeljic et al*. [2013a], the average flow speed along the *x*-direction is calculated as $\hat{U} = \hat{q} / \phi$ , where $\hat{q} = \hat{Q} / \left( \hat{L}_{im,z} \hat{L}_{im,y} \right)$ is the *x*-component of the Darcy velocity, and $\hat{Q}$ (m$^3$ /s) is the total volumetric flux.

Table S1 lists the results of the characterization of the flow conditions we investigate. We compute the Reynolds number

$$Re = \frac{\hat{\rho} \hat{U} \hat{L}}{\hat{\mu}} \tag{S3}$$

to verify the nature of the flow regime in the two images. Replacing in (S3) the length scales introduced in Section 2.2 ($\hat{L}$ = 56 μm for bead pack and $\hat{L}$ = 121 μm for sandstone) we obtain *Re* = 0.051 and *Re* = 0.125 for bead pack and Bentheimer sandstone, respectively. These values are below the threshold Reynolds number $Re_{thr}$ characterizing the onset of non-Darcy flow in the bead pack ($Re_{thr}$ = 1.562) and Bentheimer sandstone ($Re_{thr}$ = 0.170) obtained on exactly the same images as studied in our manuscript following the methodology introduced by *Muljadi et al.* [2015]. This result implies the absence of significant inertial effects. We also estimate the range $\hat{\lambda}_{vel}$ of the variogram of the modulus of the computed pore-scale velocity. Values of $\hat{\lambda}_{vel}$ listed in Table S1 are obtained by relying on an exponential model to interpret the variogram

reported by *Bijeljic et al.* [2013a]. We observe velocity values to become uncorrelated at separation distances (or lags) which are between 10 and 20% of the total sample size.

**Table S1.**

| | Geometry | | | | Flow | | | |
|---|---|---|---|---|---|---|---|---|
| | $\hat{\Delta}$ [μm] | $\hat{L}_{im}$ [μm] | $\phi$ | $\hat{\lambda}_G$ [μm] | $\hat{U}$ [mm/s] | $Re$ | $Re_{thr}$ | $\hat{\lambda}_{vel}$ [μm] |
| Bead pack | 2 | 600 | 0.359 | 48 | 0.91 | 0.051 | 1.562 | 103 |
| Sandstone | 3 | 900 | 0.215 | 121 | 1.03 | 0.125 | 0.170 | 185 |

Table S1. Characterization of pore-scale geometry and flow in the two considered pore spaces.

**Text S3. Analytical derivation of equations (9)-(11)**

We start from the pore-scale system (3)-(4) and the related boundary conditions (5). Equations (3)-(5) are expressed in terms of the local concentrations in the mobile (*M*) and immobile (*I*) regions of the elementary cell illustrated in Figure 1d-e. Our aim is to obtain an upscaled model written in term of the section-averaged concentrations:

$$\bar{M} = \frac{1}{h}\int_{-h/2}^{+h/2} M dy; \quad \bar{I} = \frac{1}{H-h}\left(\int_{-H/2}^{-h/2} I dy + \int_{h/2}^{H/2} I dy\right) \tag{S4}$$

To do so, we first average (3)-(4) along the transverse section of the system, to obtain the section-averaged equations (6)-(7). System (6)-(7) embeds local fluctuations/deviations of concentrations $\tilde{M} = M - \bar{M}$ and $\tilde{I} = I - \bar{I}$. Hence, it requires the formulation of a closure problem [e.g., *Whitaker*, 1999; *Auriault and Adler*, 1995]. In the following, we present the closure system which allows deriving the continuum-scale section-averaged system (10)-(13). We do so by relying on previous work by [e.g, *Davit et al.*, 2010; *Porta et al.* 2013] who perform theoretical upscaling for a generic three-dimensional unit cell and propose a general formulation for the closure problem for the same type of application we consider. Here, we apply the definitions described by *Porta et al.* [2013] to the simplified elementary cell represented in Figure 2.

We subtract the section-averaged equations (6)-(7) from the pore-scale system (3)-(4) to obtain:

$$\frac{\partial \tilde{M}}{\partial t} + \tilde{u}\frac{\partial \bar{M}}{\partial x} = \frac{1}{Pe}\frac{\partial^2 \tilde{M}}{\partial y^2} - \frac{2}{Peh}\frac{\partial \tilde{M}}{\partial y}\bigg|_{y=h/2} \qquad |y| < h/2 \tag{S5}$$

$$\frac{\partial \tilde{I}}{\partial t} = \frac{1}{Pe}\frac{\partial^2 \tilde{I}}{\partial y^2} + \frac{2}{Pe(1-h)}\frac{\partial \tilde{I}}{\partial y}\bigg|_{y=h/2} \qquad h/2 < |y| < 1/2 \tag{S6}$$

Here,

$$\tilde{u} = u - \frac{1}{h}\int_{-h/2}^{+h/2} u dy = u - U_M \tag{S7}$$

is the deviation of velocity from the mean value in the mobile region. Our choice of dimensionless variables (see Section 2.2) renders $U_M = 1$; $H = 1$; $0 < h < 1$. Note that system (S5)-(S6) relies on the same assumptions upon which the Taylor-Aris section-averaged transport model in a plane crack is typically grounded [*Wooding,* 1960], i.e., we assume gradients along *y* to be much larger than those along *x*. A quasi steady solution of the problem can be formulated by dropping the time derivatives in (S5)-(S6). This condition is typically formulated considering the assumption

$$\frac{\partial \tilde{M}}{\partial t} << \frac{1}{Pe}\frac{\partial^2 \tilde{M}}{\partial y^2} \qquad \frac{\partial \tilde{I}}{\partial t} << \frac{1}{Pe}\frac{\partial^2 \tilde{I}}{\partial y^2} \quad \text{for } t > t_{QS} \tag{S7}$$

where $t_{QS}$ is a threshold time. The time derivatives can be disregarded when $t_{QS} \to 0$. Taking into account the time variation of the closure variables implies that the resulting upscaled equation contains nonlocal (integrodifferential) terms [*Moyne*, 1997; *Chastanet and Wood*, 2008; *Porta et al.,* 2013]. Here we aim at limiting model complexity and choose to drop the time derivatives in (S5)-(S6) to assume a quasi steady approximation of the system. Our results in Section 3 suggest that this is an acceptable assumption for the settings investigated in this study. The boundary conditions which are needed to solve system (S5)-(S6) stem from (5) and are expressed as:

$$\frac{\partial \tilde{M}}{\partial y} = \frac{\partial \tilde{I}}{\partial y} \quad ; \quad \tilde{M} = \tilde{I} - \Delta\overline{c} \quad with \quad \Delta\overline{c} = \overline{M} - \overline{I} \qquad |y| = h/2 \tag{S8}$$

$$\frac{\partial \tilde{I}}{\partial y} = 0 \qquad |y| = 1/2 \tag{S9}$$

Equations (S5)-(S9) form a system of coupled equations, which are linear with respect to the unknowns $\tilde{M}$ and $\tilde{I}$. Upon relying on the superposition principle of linear operators [e.g., *Whitaker*, 1999; *Davit et al.*, 2010] we express the solution of system (S5)-(S9) as:

$$\tilde{M} = b_1(y)\frac{\partial \overline{M}}{\partial x} + b_3(y)\Delta\overline{c} \tag{S10}$$

$$\tilde{I} = b_2(y)\frac{\partial \overline{M}}{\partial x} + b_4(y)\Delta\overline{c} \tag{S11}$$

Here $b_i$ ($i$ = 1,...,4) are closure variables. Replacing (S10)-(S11) into (S5)-(S9) we obtain the following two systems of equations:

$$\begin{cases} \dfrac{\partial b_1}{\partial t} + \tilde{u} = \dfrac{1}{Pe}\dfrac{\partial^2 b_1}{\partial y^2} - \dfrac{2}{Peh}\dfrac{\partial b_1}{\partial y}\Big|_{y=h/2} & |y| < h/2 \\ \dfrac{\partial b_2}{\partial t} = \dfrac{1}{Pe}\dfrac{\partial^2 b_2}{\partial y^2} + \dfrac{2}{Pe(1-h)}\dfrac{\partial b_2}{\partial y}\Big|_{y=h/2} & h/2 < |y| < 1/2 \\ b_1 = b_2;\ \dfrac{\partial b_1}{\partial y} = \dfrac{\partial b_2}{\partial y} & |y| = h/2 \\ \dfrac{\partial b_2}{\partial y} = 0 & |y| = 1/2 \end{cases} \tag{S12}$$

$$\begin{cases} \dfrac{\partial b_3}{\partial t} = \dfrac{1}{Pe}\dfrac{\partial^2 b_3}{\partial y^2} - \dfrac{2}{Peh}\dfrac{\partial b_3}{\partial y}\bigg|_{y=h/2} & |y| < h/2 \\ \dfrac{\partial b_4}{\partial t} = \dfrac{1}{Pe}\dfrac{\partial^2 b_4}{\partial y^2} + \dfrac{2}{Pe(1-h)}\dfrac{\partial b_4}{\partial y}\bigg|_{y=h/2} & h/2 < |y| < 1/2 \\ b_3 = b_4 - 1; \dfrac{\partial b_3}{\partial y} = \dfrac{\partial b_4}{\partial y} & |y| = h/2 \\ \dfrac{\partial b_4}{\partial y} = 0 & |y| = 1/2 \end{cases} \tag{S13}$$

Solving (S12)-(S13) requires all closure variables to have zero mean, i.e., $\overline{b_i} = 0$ ($i$ = 1, ..., 4). This ensures $\overline{\tilde{M}} = 0; \overline{\tilde{I}} = 0$ for any pair $\dfrac{\partial \overline{M}}{\partial x}, \Delta\overline{c}$. Systems (S12)-(S13) are not coupled. They are characterized by a very similar structure and can be readily solved for $0 < h < 1$. The key difference between (S12) and (S13) is that the fluctuation of velocity $\tilde{u}$ appears in the first of (S12), while the solution of (S13) does not depend on velocity. Therefore, the distribution of closure variables $b_1$ and $b_2$ along $y$ is influenced by $\tilde{u}$ and $h$, while $b_3$ and $b_4$ depend solely on $h$ and can be solved analytically independent of the assumed velocity distribution. The analytical solution of (S13) is:

$$b_3 = \frac{1}{2h} - \frac{6}{h}y^2 \tag{S14}$$

$$b_4 = \frac{h^2 - 2h - 2}{2(1-h)} + \frac{6y(y-1)}{1-h} \tag{S15}$$

In this work we propose two possible choices to characterize the velocity deviation, $\tilde{u}$, in the mobile region of the unit cell: (*i*) Poiseuille flow distribution (model 1, see Figure 2a), (*ii*) velocity distribution derived from the probability distribution of pore-scale simulated velocities (model 2, Figure 2b). The solution of system (S12) can be evaluated analytically only when $\tilde{u}$ is a known function of $y$. Otherwise, a numerical solution is required.

When Poiseuille flow is assumed in the mobile region (model 1) we set

$$\tilde{u} = \frac{1}{2} - 6\frac{y^2}{h^2} \tag{S16}$$

Replacing (S16) in (S12) yields

$$b_1 = Pe\left(-\frac{y^4}{2h^2} + \frac{y^2}{4} - \frac{y^2 h}{10} - \frac{7h^2}{480} + \frac{h^3}{120}\right) \tag{S17}$$

$$b_2 = Pe\left(\frac{h^4 - 2h^3 - 2h^2}{120(1-h)} + \frac{y(y-1)h^2}{10(1-h)}\right) \tag{S18}$$

In the case of model 2, we compute the closure variables $b_1$ and $b_2$ by numerical integration of (S13). We do so via a standard centered finite difference scheme.
Substituting the closure expressions (S10)-(S11) into the section-averaged equations (6)-(7) and considering $(1-h)=\gamma_I$ and $h=\gamma_M$ leads to

$$\frac{\partial \bar{M}}{\partial t}+\frac{\partial \bar{M}}{\partial x}+\frac{\partial}{\partial x}\left(\overline{\tilde{u}b_1}\frac{\partial \bar{M}}{\partial x}+\overline{\tilde{u}b_3}\Delta\bar{c}\right)=\frac{1}{Pe}\frac{\partial^2 \bar{M}}{\partial x^2}+\frac{2}{Pe\gamma_M}\left(\left.\frac{\partial b_1}{\partial y}\right|_{y=h/2}\frac{\partial \bar{M}}{\partial x}+\left.\frac{\partial b_3}{\partial y}\right|_{y=h/2}\Delta\bar{c}\right) \quad \text{(S19)}$$

$$\frac{\partial \bar{I}}{\partial t}=\frac{1}{Pe}\frac{\partial^2 \bar{I}}{\partial x^2}-\frac{2}{Pe\gamma_I}\left(\left.\frac{\partial b_2}{\partial y}\right|_{y=h/2}\frac{\partial \bar{M}}{\partial x}+\left.\frac{\partial b_4}{\partial y}\right|_{y=h/2}\Delta\bar{c}\right) \quad \text{(S20)}$$

Finally, a suitable rearrangement of the terms in (S19)-(S20) leads to the system (9)-(11), which is here reported for convenience:

$$\frac{\partial \bar{M}}{\partial t}+\frac{\partial \bar{M}}{\partial x}+\frac{\partial}{\partial x}\left[d_{H1}\frac{\partial \bar{M}}{\partial x}+d_{H2}\Delta\bar{c}\right]=\frac{1}{Pe}\frac{\partial^2 \bar{M}}{\partial x^2}+\frac{1}{Pe\gamma_M}\left(e_1\frac{\partial \bar{M}}{\partial x}+e_2\Delta\bar{c}\right) \quad \text{(S21)}$$

$$\frac{\partial \bar{I}}{\partial t}=\frac{1}{Pe}\frac{\partial^2 \bar{I}}{\partial x^2}+\frac{1}{Pe\gamma_I}\left(e_1\frac{\partial \bar{M}}{\partial x}+e_2\Delta\bar{c}\right) \quad \text{(S22)}$$

$$d_{H1}=\frac{1}{h}\int_{-h/2}^{h/2}b_1\tilde{u}\,dy \qquad d_{H2}=\frac{1}{h}\int_{-h/2}^{h/2}b_3\tilde{u}\,dy \qquad e_1=2\left.\frac{\partial b_2}{\partial y}\right|_{y=h/2} \qquad e_2=2\left.\frac{\partial b_4}{\partial y}\right|_{y=h/2} \quad \text{(S23)}$$

Table 1 lists the value of the coefficients (S23), which are employed to compute the results illustrated in Section 3.
Finally, we compare the results given by model 2 for selected threshold values of $Pe_{thr}$, which is the quantity employed to demarcate mobile and immobile regions (see Section 2). Figure S1 depicts a comparison of the longitudinal profiles (along $x$-direction) of section-averaged concentrations obtained when $Pe_{thr}$ = 1, 10, 15, 30. Figure S2 depicts the influence of $Pe_{thr}$ on the dilution index $DI$. Both figures reveal that for the sandstone sample the results are not particularly sensitive to $Pe_{thr}$ when $1 < Pe_{thr} < 30$. Otherwise, the results associated with the bead pack sample tend to become particularly sensitive to the value of $Pe_{thr}$, when $Pe_{thr} > 10$. We note that the average value of $Pe(\hat{\mathbf{x}})$ for the bead pack is 23.4, with a median value of about 20 and that $Pe_{thr}$ = 15 already implies that advective effects are more than one order of magnitude stronger than diffusive effects. As such, considering values of $Pe_{thr} > 15$ is not entirely consistent with the key premises of our simple interpretive model. We observe that for both samples results are not sensitive to the selected value of $Pe_{thr}$ for $1 \le Pe_{thr} \le 10$.

**Table S2.**

| | | | Model 1 | | | | Model 2 | | | |
|---|---|---|---|---|---|---|---|---|---|---|
| | $\gamma_M$ | $Pe$ | $d_{H1}$ | $d_{H2}$ | $e_1$ | $e_2$ | $d_{H1}$ | $d_{H2}$ | $e_1$ | $e_2$ |
| Bead pack | 0.73 | 31.8 | -0.04 | 0.14 | -1.69 | -12 | -0.08 | 0.17 | -1.85 | -12 |
| Sandstone | 0.75 | 75.2 | -0.09 | 0.15 | -4.23 | -12 | -0.55 | 0.25 | -7.02 | -12 |

Table S2. Values of the parameters (S23) for the two porous samples as rendered by our two modeling choices.

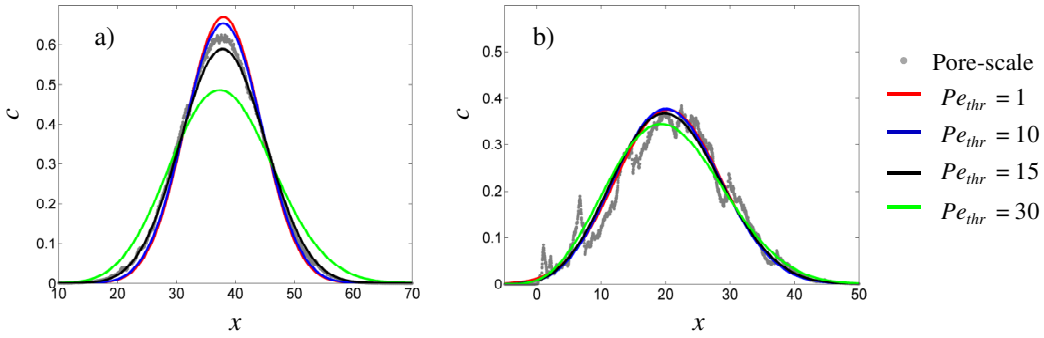


Figure S1. Comparison of section-averaged concentrations rendered by pore-scale particle tracking and our model 2 for selected values of $Pe_{thr}$, for (a) the bead pack and (b) the sandstone samples at $\hat{t}$ = 2 s.

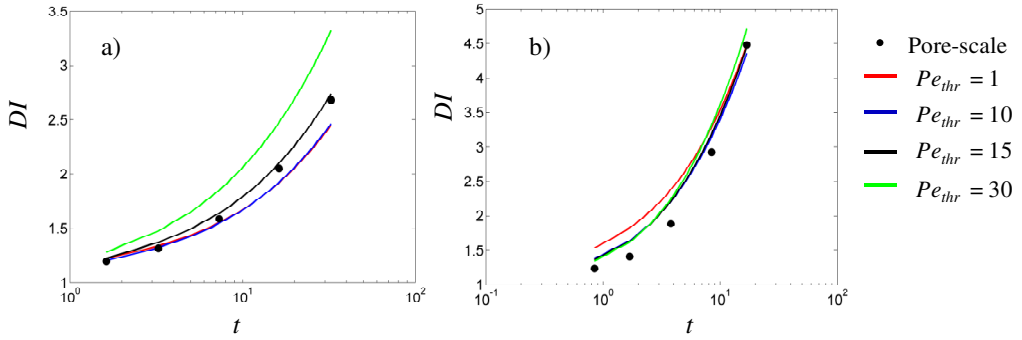


Figure S2. Time evolution of the dilution index obtained by pore-scale particle tracking and our model 2 for selected values of $Pe_{thr}$, for (a) the bead pack and (b) the sandstone samples.

## References


Alhashmi Z., M. J. Blunt and B. Bijeljic (2015). Predictions of Dynamic Changes in Reaction Rates as a Consequence of Incomplete Mixing Using Pore-scale Reactive Transport Modeling on Images of Porous Media, *J. Contam. Hydrol.*, http://dx.doi.org/10.1016/ j.jconhyd.2015.06.004.

Auriault, J.-L., and P.M. Adler (1995), Taylor dispersion in porous media: Analysis by multiple scale expansions, *Adv. Water Resour.,* 18, 217-226.

Bijeljic, B., A. Raeini, P. Mostaghimi and M. J. Blunt (2013a), Predictions of non-Fickian solute transport in different classes of porous media using direct simulation on pore-scale images, *Phys. Rev. E*, 87, 013011, doi:10.1103/PhysRevE.87.013011.

Bijeljic, B., P. Mostaghimi, and M. J. Blunt (2013b), Insights into non-Fickian solute transport in carbonates, *Water Resour. Res.*, 49, 2714–2728, doi:10.1002/wrcr.20238.

Chastanet, J., and B.D. Wood (2008), Mass transfer process in a two-region medium, *Water Resour. Res*., 44, W05413.

Davit, Y., M. Quintard, and G. Debenest (2010), Equivalence between volume averaging and moments matching techniques for mass transport models in porous media. *Int. J. Heat Mass Tran*., 53(21), 4985–4993.

Finney, J. L. (1970), Random packings and the structure of simple liquids I. The geometry of random close packing. Proc. *R. Soc. London, Ser. A* , 319, 479-493.

Issa, R. (1986), Solution of the implicitly discretised fluid flow equations by operator-splitting, *J. Comput. Phys.*, 62(1), 40-65.

Moyne, C., (1997), Two-equation model for a diffusive process in porous media using the volume averaging method with an unsteady-state closure, *Adv. Water Resour.*, 20, 63-76.

Muljadi, A., M. J. Blunt, Q. A. Raeini and B. Bijeljic (2015), On the Onset of Non-Darcy Flow in Heterogeneous Porous Media, *Adv. Water Resour.* doi:10.1016/j.advwatres.2015.05.019.

Pereira Nunes, J. P., B. Bijeljic and M. J. Blunt (2015), Time-of-Flight Distributions and Breakthrough Curves in Heterogeneous Porous Media Using a Pore-Scale Streamline Tracing Algorithm, *Transp. Porous Med.* doi:10.1007/s11242-015-0520-y.

Porta, G., S. Chaynikov, M. Riva, and A. Guadagnini (2013), Upscaling solute transport in porous media from the pore-scale to dual- and multicontinuum formulations, *Water Resour. Res*., 49(4), 2025-39, doi:10.1002/wrcr.20183.

Prodanović, M. and S. L. Bryant (2006), A level set method for determining critical curvatures for drainage and imbibition. *J. Colloid Interf. Sci.*, 304, 442-458.

Raeini, A. Q., Blunt, M. J. and B. Bijeljic (2012), Modelling two-phase flow in porous media at the pore-scale using the volume-of-fluid method. *J. Comput. Phys.*, 231, 5653-5668.

Scheven, U. M., D. Verganelakis, R. Harris, M. L. Johns, and L. F. Gladden (2005), Quantitative nuclear magnetic resonance measurements of preasymptotic dispersion in flow through porous media, *Phys. Fluids*, 17, 117107.

Siena, M., A. Guadagnini, M. Riva, B. Bijeljic, J. P. Pereira Nunes, and M. J. Blunt (2014) Statistical scaling of pore-scale Lagrangian velocities in natural porous media, *Phys. Rev. E*, 90, 023013.

Whitaker, S. (1999), The method of volume averaging, *Netherlands: Kluwer Academic Publishers.*

Wooding, R. A., (1960), Instability of a viscous fluid of variable density in a vertical Hele-Shaw cell, *J. Fluid Mech.* 7, 501-515.